

Cite this: *J. Mater. Chem. A*, 2019, 7, 14455Received 3rd April 2019
Accepted 28th May 2019

DOI: 10.1039/c9ta03542g

rsc.li/materials-a

The 3d–5d orbital repulsion of transition metals in oxyhydroxide catalysts facilitates water oxidation†

Lie Wang,^{‡a} Yunzhou Wen,^{‡a} Yujin Ji,^{‡b} Hanjie Cao,^c Shangyu Li,^a Sisi He,^a Haipeng Bai,^a Gejun Liu,^a Longsheng Zhang,^a Hongliang Bao,^c Jianqiang Wang,^{‡cd} Youyong Li,^{‡*b} Bo Zhang^{*a} and Huisheng Peng^{‡*a}

The electrocatalytic oxygen-evolution reaction (OER) is expected to play a vital role in the development of electrochemical energy conversion and storage technologies. 3d transition-metal oxyhydroxides have been reported to outperform noble metal-based catalysts for the OER, but the relatively localized properties of 3d electrons limit the sufficient modulation of their electronic structures by dopants, which may inhibit further improvement of their OER performances. Herein, through density functional theory (DFT) calculation, we found that 5d transition metals such as iridium (Ir) with unique electronic properties can effectively modulate 3d transition-metal oxyhydroxides, thus producing versatile electronic structures to facilitate the OER activity. We therefore synthesized NiFe(3d)Ir(5d) oxyhydroxides and explored their electronic structures *via in situ* and *ex situ* X-ray absorption spectroscopy (XAS) and valence band X-ray photoelectron spectroscopy (VB-XPS). The DFT, XAS, VB-XPS and electrochemical studies demonstrated that Ir served as a modulator in the 3d metal oxyhydroxide framework, and created a local environment favoring 3d–5d orbital interaction, and the repelled Ni 3d orbitals facilitated the overall OER process. The Ir-doped catalyst on a glassy carbon electrode delivers 133 mV lower overpotential to achieve a current density of 10 mA cm⁻² in an alkaline electrolyte, a 53-fold improved turnover frequency (TOF) over that of pristine NiFe oxyhydroxides, with negligible activity decay after 500 hours of operation.

Converting renewable energy into high value-added, energy-dense chemicals *via* electrochemical methods, including

electrochemical water splitting,^{1–3} CO₂ and CO reduction,^{4,5} and ammonia synthesis,⁶ has received increasing research attention in recent years. Among the above electrochemical energy conversion and storage approaches, one major obstacle that inhibits the further improvement of electrical-to-chemical energy conversion efficiency is the sluggish four-electron kinetics of the anodic oxygen evolution reaction (OER). This reaction often demands a large overpotential to achieve the desired current densities of ≥ 10 mA cm⁻² even under catalysis with the most efficient noble-metal catalysts.

Recently, utilizing earth-abundant first-row (3d) transition-metal catalysts including oxides,⁷ oxyhydroxides,⁷ sulfides,⁸ phosphides,^{8,9} perovskites^{10,11} and metal–organic framework^{12,13} compounds as OER electrocatalysts in alkaline media has aroused increasing interest. It has been theoretically reported that by precisely modulating the 3d electronic structures, these 3d transition-metal catalysts have the potential to reach the vertex of the oxygen evolution volcano limits. In this perspective, numerous efforts have been made to adjust 3d metal electronic structures to an OER-favoring state, such as modifying the e_g filling status of Mn-based perovskite oxides (ABO₃) through Ca and Yb ratio changes at the A site¹¹ and introducing 3d-metal vanadium ions into the NiFe layered double hydroxide.¹⁴ However, in oxides/hydroxides, 3d orbitals usually demonstrate relatively localized properties of electrons, in which the Coulomb interaction overwhelms other interactions such as crystal field effects and band formation.¹⁵ This could possibly reduce the chance to effectively modulate the electronic structures through other 3d metal dopants for the OER.

In contrast, 5d transition metals possess increased 5d electronic wave function spatial extent,¹⁶ which might modulate the neighboring 3d transition metals in multi-metal oxides/hydroxides. For example, a recently reported 5d-metal doped FeCoW electrocatalyst outperformed noble metal-based catalysts towards the OER.¹⁷ Thus we propose that 5d transition metals could modulate 3d transition-metal oxyhydroxides *via* the interaction between 3d and 5d orbitals, producing versatile electronic structures that can enhance the OER activity. Among

^aState Key Laboratory of Molecular Engineering of Polymers, Department of Macromolecular Science, Laboratory of Advanced Materials, Fudan University, Shanghai, 200438, China. E-mail: penghs@fudan.edu.cn; bozhang@fudan.edu.cn

^bInstitute of Functional Nano & Soft Materials (FUNSOM), Jiangsu Key Laboratory for Carbon-Based Functional Materials & Devices, Soochow University, Suzhou, 215123, China. E-mail: yyli@suda.edu.cn

^cShanghai Institute of Applied Physics, Chinese Academy of Sciences, Shanghai, 201800, China

^dDalian National Laboratory for Clean Energy, Dalian, 116023, China

† Electronic supplementary information (ESI) available. See DOI: 10.1039/c9ta03542g

‡ These authors contributed equally to this work.

all the 5d transition-metals, iridium (Ir) was highlighted not only because it is a good OER catalyst itself, but also because it has unique electronic structures,¹⁸ *i.e.*, weak electronic correlations ($U \sim 0.5\text{--}3$ eV), strong crystal field effects ($CF \sim 1\text{--}5$ eV) and strong spin-orbit coupling effects ($SO \sim 0.1\text{--}1$ eV). The close correspondence of these energy scales provides more degrees of freedom for elaborately tuning the electronic structures of host materials.¹⁹ We therefore explored combinations of 5d transition metal Ir and 3d transition metal Ni and Fe to modulate their electronic structures and local coordination environment with the goal of improving the OER activity.

First-principles calculations were implemented first to investigate the electrocatalytic activity of (Ir, Fe) atom doped oxyhydroxide materials (NiOOH) (Fig. 1) and the concrete OER mechanisms were also compared on pristine NiOOH and IrO₂ surfaces. For pristine NiOOH surfaces, our results show that the formation of an O radical was the determining step with an

energy barrier of 1.99 eV and the calculated onset potential was 0.76 V, which agreed with that in the previous work.²⁰ After the introduction of (Ir, Fe) atoms, the O radical was favorably adsorbed on the Ir site while O–O coupling catalyzed by the Ni site was further accelerated, leading to an obviously improved OER process with a lower energy barrier (1.48 eV) and a lower onset potential (0.25 V). Compared with the Fe-doped NiOOH, the theoretical onset potential of Ir, Fe-doped NiOOH is also decreased by 0.2 V.²⁰ Thus, the valence orbital (5d) of the dopant Ir might interact with the neighboring Ni's valence orbital (3d) *via* O atoms and, at the same time, accelerate the determining step, which contributed to the final improved OER activity. As for the IrO₂ surface, the second deprotonation process was the potential determining step with an energy barrier of 1.68 eV. Based on the initial analysis on the free energy evolution of these three configurations, we concluded that Ir doping was an effective method to improve the OER activity. The same results were also observed in Goddard III's work while the potential enhancement mechanisms have not yet been revealed.²⁰

Based on DFT calculation results, we experimentally incorporated Ir into the well-known efficient 3d NiFe oxyhydroxide catalysts and studied the effect of the Ir dopant on 3d transition multi-metal catalysts. The NiFe oxyhydroxide and Ir-doped NiFe oxyhydroxide were denoted as NiFe and NiFeIr, respectively. The high-resolution transmission electron microscopy images and energy dispersive X-ray spectrometry mapping indicated that Ni, Fe and Ir were homogeneously distributed in the oxide (Fig. S1–3†). The synthesis details are described in the Experimental section in the ESI.† To investigate the local coordination environment and atomic arrangement of post-OER Ir-doped catalysts, the extended X-ray absorption fine structure (EXAFS) measurements were first conducted. The experiments and simulations are presented in Fig. 2a and Table S1.† The rutile-structure model was found to fit the coordination environments of Ir in IrO₂ well. Six (5.93 by calculations) Ir–O bonds coordinate with the central Ir atom to form an octahedron in the first shell, with a bond length of 1.98 Å. The second shell consisted of 5.59 Ir–Ir bonds with a length of 3.14 Å. As for the NiFeIr sample, the first shell of Ir–O showed a tiny variation with IrO₂, but the second shell exhibited a ~ 0.1 Å shorter scattering path compared to Ir–Ir bonds. Considering the smaller ionic radius of Ni ions (0.48–0.56 Å) than of Ir (0.57–0.68 Å),²¹ it can be speculated that the shortened scattering peak might come from the adjacent Ni ions, *i.e.*, forming an Ir–O–Ni local coordination structure. The above results demonstrated that Ir was doped into the NiFe framework successfully. With Ir located adjacent to NiFe, Ir 5d orbitals may have the opportunity to interact with the metal 3d orbitals.

To further investigate the electronic structure of the above catalysts, the *ex situ* X-ray absorption near edge structure (XANES) spectra of post-OER catalysts at the Ir L₃-edge were studied. As shown in Fig. 2b, the absorption edge energy of Ir in NiFeIr was shifted to a lower energy by ~ 0.5 eV, located between that of IrCl₃ and IrO₂, demonstrating an oxidation state between +3 and +4. Since the white-line position of the Ir L₃-edge corresponds to the oxidation state of Ir, we quantified the formal oxidation state of NiFeIr by calculating a calibration line

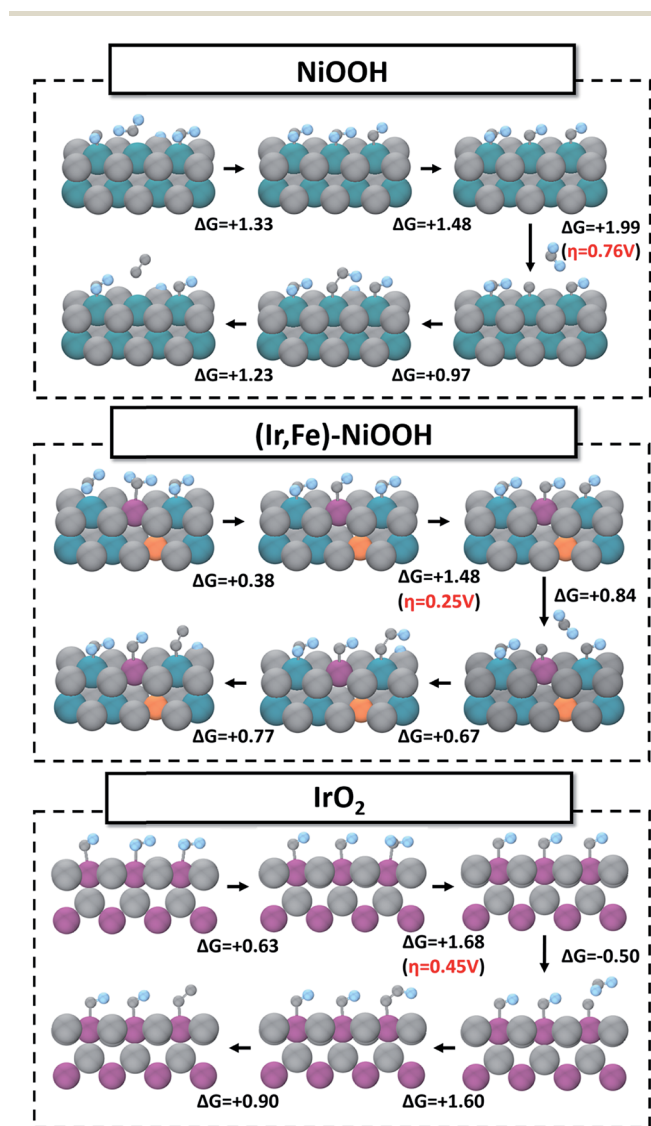


Fig. 1 The concrete OER pathway on NiOOH, Ir, Fe-doped NiOOH and IrO₂ electrocatalysts. Green balls – Ni, purple balls – Ir, orange balls – Fe, grey balls – O, and cyan balls – H.

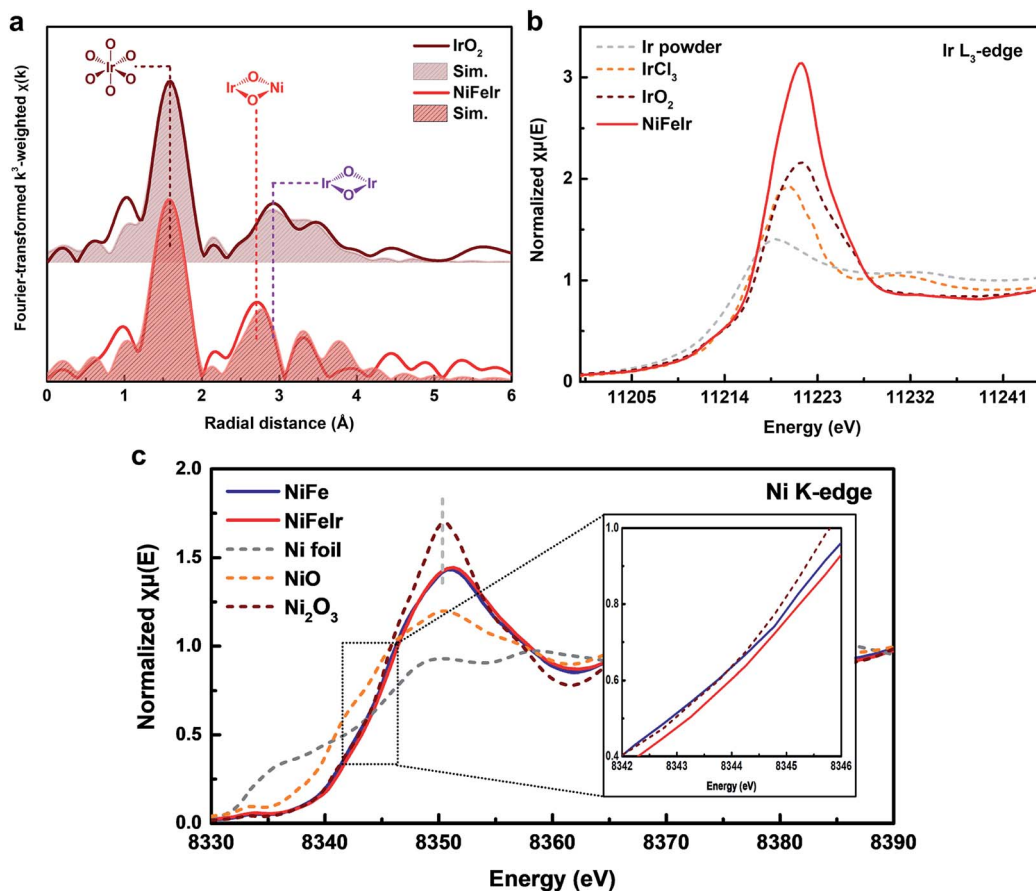


Fig. 2 (a) k^3 -weighted Fourier transforms of EXAFS spectra collected at the Ir L_3 -edge together with the simulation spectra. (b) XANES spectra of the Ir L_3 -edge of different catalysts. (c) Ni K-edge XANES spectra. Inset: enlarged portion of the near-edge region.

(Fig. S4†).^{19,22,23} According to the calibrated slope of 1.292 eV per d-electron hole, the formal oxidation state of Ir in NiFeIr is +3.82, indicating a possible electron transfer from Ni to Ir, which might be induced by the 3d–5d orbital interactions.

Modulated by Ir, the electronic structure variations of active Ni sites before and after Ir doping were investigated *via* Ni K-edge XANES spectra. As shown in Fig. 2c, both NiFe and NiFeIr demonstrated oxidation states higher than those of the Ni_2O_3 reference (Fig. 2c inset), indicating the presence of $\text{Ni}(\text{iv})$, and the absorption edge of NiFeIr was 0.5 eV higher than NiFe. These experimental results showed that there were more $\text{Ni}(\text{iv})$ sites in NiFeIr than in NiFe. Considering that high-valence metal sites $\text{Ni}(\text{iv})$ could boost the OER kinetics,^{24–26} the increased $\text{Ni}(\text{iv})$ numbers could possibly result in higher potential OER activity of the NiFeIr sample. This conclusion also agreed well with our DFT predictions.

In addition to Ni and Ir, Fe K-edge XAS spectra were also collected to study whether the introduction of Ir affected the electronic structure of Fe (Fig. S10 and 11†). However, Fe remained in the +3 state before and after Ir incorporation, and no other obvious electronic and coordination structure deviations could be identified among the different samples, which coincided with the previous reports on Ni–Fe OER catalysts. Besides, no valence change occurred for Fe before and after the

OER, which was consistent with the previous reports.^{25,27} The role of iron has been studied in many literature reports in which the existence of iron promoted the formation of $\text{Ni}(\text{iv})$ or diminished the charge contribution process of $\text{Ni}(\text{iv})$.^{25,26}

To uncover the inherent relationship between the high predicted catalytic performance and the 5d-Ir-modulated NiFe catalysts' electronic structures, we adopted an in-depth investigation to the experimental and theoretical results at the electronic level. Firstly, by differentiating the Ir L_3 -edge XANES spectra (Fig. 3a), two negative spikes located at 11218.8 and 11221.7 eV were resolved, attributed to the empty states of t_{2g} and e_g bands, respectively.²² In the NiFeIr sample, the white-line shifted to lower energy and the e_g absorption peak was significantly larger than the t_{2g} peak, indicating that the total 5d orbital energy decreased and Ir possessed a low-spin d-electron configuration ($t_{2g}^5 e_g^0$). However in IrO_2 samples, the t_{2g} and e_g peaks were of similar area, indicating a high-spin d-electron configuration ($t_{2g}^3 e_g^2$). Valence band X-ray photoelectron spectroscopy (VB-XPS) was then carried out to probe the Frontier orbitals' deviation before and after Ir doping (Fig. 3b). Compared to that of pure NiFe, the valence band of NiFeIr shifted to a higher binding energy. Combining the above results, we hypothesized that neighboring 3d and 5d orbitals would repelled each other, thus changing the orbital energy and

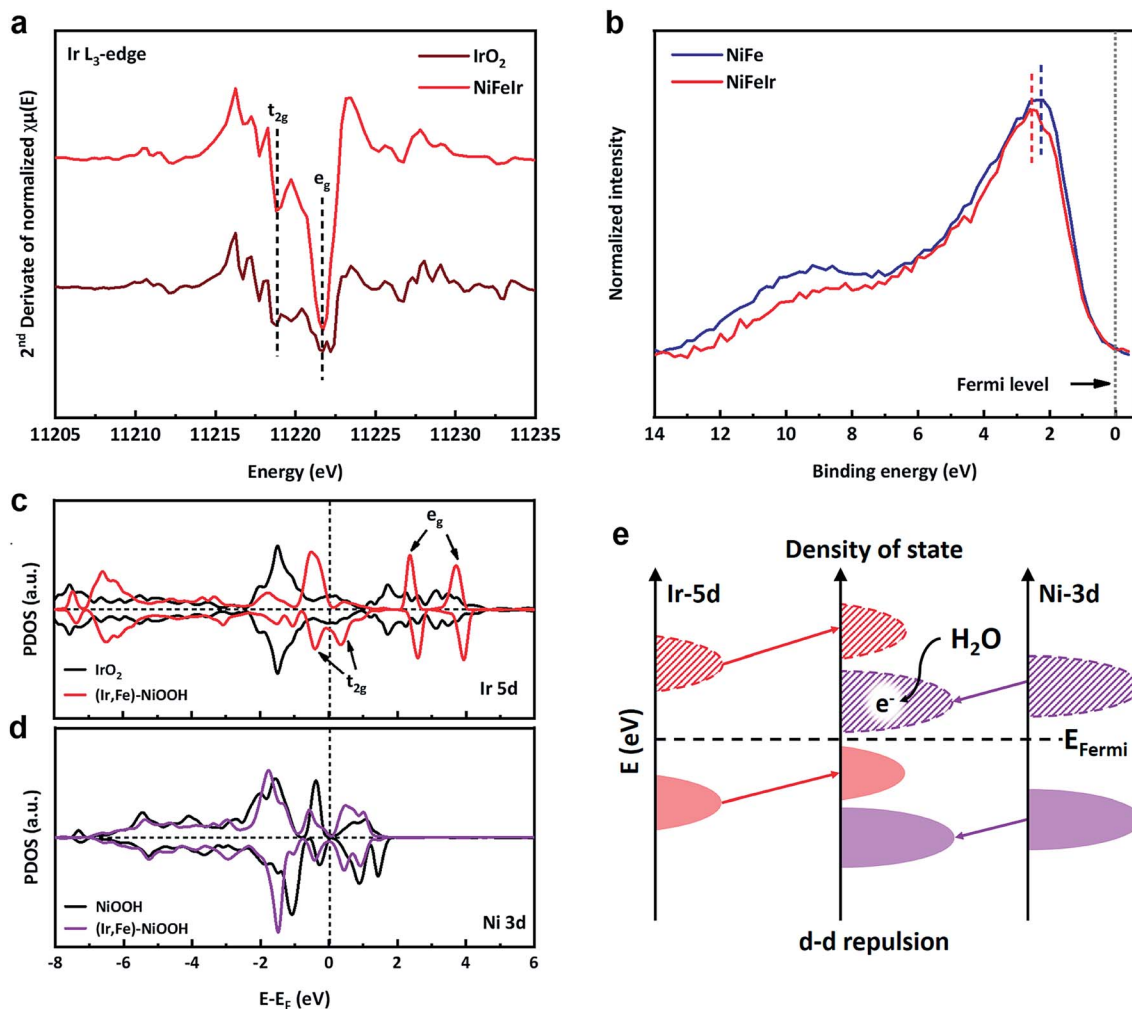


Fig. 3 (a) Second derivative of normalized Ir L₃-edge XANES. (b) VB-XPS spectra of NiFe and NiFeIr after baseline subtraction. (c) PDOS of the 5d orbitals of Ir in IrO₂ and (Ir, Fe)-NiOOH. (d) PDOS of the 3d orbitals of Ni in NiOOH and (Ir, Fe)-NiOOH. (e) Schematic of d-d orbital repulsion of Ir–Ni when Ir–Ni co-existed in the neighboring sites. The dashed line, shaded area and solid area refer to the Fermi level, unoccupied states and occupied states, respectively.

electronic configurations. To verify our hypothesis, we examined projected density of states (PDOS) of different catalyst models. As shown in Fig. 3c and d, the d band peak of the Ir atom in pristine IrO₂ had a higher energy level than that of the Ni atom in pristine NiOOH. When Ni and Ir coexisted in the neighboring sites, the d-d orbital repulsion would shift the d band peak of the Ni atom to lower unoccupied and occupied states. Meanwhile, the d orbitals of Ir were pushed to a higher energy level in contrast, and the electrons in iridium e_g states were repelled to t_{2g} states, resulting in the increasing unoccupied e_g states. These energy variations matched well with experimental spectroscopy results, and could facilitate the overall OER process. With the 3d orbital repelled to a lower energy level, more highly active Ni(IV) might be generated.^{28,29} The modified Ni site may stabilize the adsorption of *OH intermediates and increase the possibility of O–O coupling.^{30–33} The increased energy level of Ir might decrease the formation energy barrier of O radicals.²⁰ A schematic of the d-d repulsion interaction is presented in Fig. 3e.

We then sought to characterize the catalytic performance of NiFe, NiFeIr and IrO₂ in a 1 M KOH electrolyte at room temperature (see Experimental section for details).[†] As shown in Fig. 4a and S12,[†] the NiFeIr required an overpotential of 255 mV to achieve a current density of 10 mA cm⁻², significantly lower than those of NiFe (340 mV) and IrO₂ (323 mV) (Table S3[†]), confirming the validation of the d-d repulsion interaction in an Ir-modulated NiFe catalyst. Many previous studies reported that bulk/surface amorphization of materials led to better OER performance in alkaline media.^{17,34} With this in mind, we further optimized the catalytic activity of NiFeIr prepared *via* the annealing-free sol-gel process (labeled NiFeIr-RT), which can result in homogeneous metal distribution with lower crystallinity (Fig. S13 and S14d[†]).¹⁷ The overpotential of NiFeIr-RT can be further decreased to 207 mV (Fig. 4a and S12[†]), which is superior to that of most recently reported high-performance electrocatalysts (Fig. 4b and also see the comparison in Table S4[†]). A significant feature in the NiFeIr-RT polarization curve was that the oxidation peak of Ni(II) to

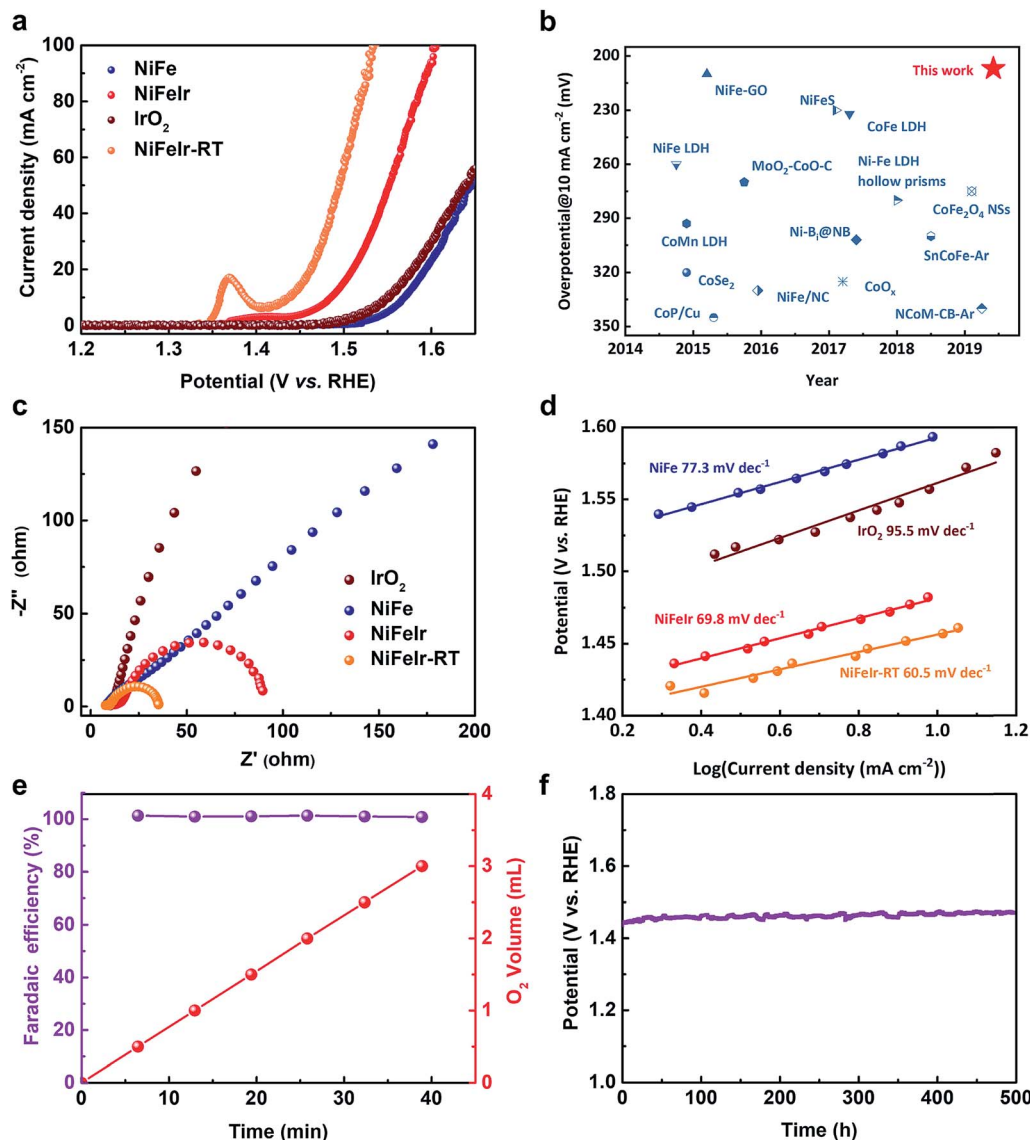


Fig. 4 (a) The OER polarization curves for different electrocatalysts in a 1 M KOH solution. (b) Comparison of the overpotential in this work with that of recent catalysts in 1 M KOH. (c) Nyquist plots for different electrocatalysts recorded at 1.48 V vs. RHE. (d) The Tafel slopes of different electrocatalysts. (e) Amount of O₂ experimentally measured and faradaic efficiency versus time for NiFeIr-RT. (f) Chronopotentiometric durability of NiFeIr-RT with a constant current density of 10 mA cm⁻².

Ni(III)/Ni(IV) increased sharply, indicating more Ni(III)/Ni(IV) sites were generated in the amorphous sample. This result was further verified by *in situ* and *ex situ* XAFS and XPS studies (Fig. S15–20†). Meanwhile, the Ir e_g state changes and valence band deviations could still be observed, and the d–d repulsion was retained and reinforced after the amorphization (Fig. S21 and S22†). These phenomena could be possibly explained by the increased possibility of the Ni 3d and Ir 5d interactions in the amorphous sample, which contributed to the enhanced OER performance. In addition, the valence of Fe in NiFeIr-RT remains stable before and after the reaction (Fig. S23 and S24†), which was consistent with the above results.

Electrochemical impedance spectroscopy (EIS) of the catalysts was then performed. Both NiFeIr and NiFeIr-RT catalysts showed significantly smaller Nyquist semicircle diameters than

NiFe and IrO₂ (Fig. 4c and S25–29†). The charge transfer resistances R_{ct} of NiFeIr and NiFeIr-RT were smaller (Table S2†), which indicated faster interfacial charge transfer with a superior catalytic activity. Moreover, the Tafel slopes of NiFeIr and NiFeIr-RT were 69.8 and 60.5 mV dec⁻¹, respectively, smaller than those of the other catalysts (77.3 and 95.5 mV dec⁻¹), further demonstrating that Ir incorporation indeed improved the OER activity for NiFe (Fig. 4d). In order to investigate whether the OER activity of NiFeIr and NiFeIr-RT originated from intrinsic catalytic properties of multi-metal active sites or exclusively from an enhanced surface area, the electrochemical surface areas (ECSAs) were further estimated (Fig. S30 and 31 and Table S3†). The specific activity confirmed that the intrinsic activities of Ir-modulated Ni sites (NiFeIr and NiFeIr-RT) were notably higher than those of NiFe and IrO₂ (Fig. S32†). The

intrinsic activity was also confirmed by determining the TOFs for this catalyst. As shown in Table S3,† the NiFeIr and NiFeIr-RT catalysts exhibited much higher TOFs of 2.09 s^{-1} and 12.69 s^{-1} , which are 9-fold and 53-fold improvements compared with those of the pristine NiFe oxyhydroxides, respectively (normalized by C_{dl} obtained from cyclic voltammetry).

Furthermore, the faradaic efficiency was determined by comparing the total charge passed with the corresponding amount of evolved O_2 . As shown in Fig. 4e, the faradaic efficiency of the NiFeIr-RT catalyst was nearly 100%. To estimate the stability, we ran a chronopotentiometric test on the water oxidation of the NiFeIr-RT catalyst with a constant current density of 10 mA cm^{-2} . The potential did not obviously increase for about 500 h, suggesting a high operating stability (Fig. 4f).

In conclusion, we have developed a powerful strategy to achieve a high-efficiency NiFeIr electrocatalyst for water oxidation by using 3d–5d orbital repulsion to tune the electronic structures, combining DFT calculations and experimental verifications. As a result, an extraordinarily low OER overpotential of 207 mV and high TOF of 12.69 s^{-1} on a glassy carbon electrode have been achieved, superior to those of the benchmark pristine NiFe and IrO_2 catalysts. This 3d–5d orbital interaction strategy not only provides an avenue to high-efficiency water oxidation, but may also be extended to improve the performance of other multi-metal catalysts.

Conflicts of interest

The authors declare no conflict of interest.

Acknowledgements

This work was supported by the MOST (2016YFA0203302), NSFC (21634003, 51573027, 51673043, 21604012, 21805044, and 21875042), STCSM (16JC1400702, 17QA1400400, 18QA1400700, 18QA1400800, and 19QA1400800), SHMEC (2017-01-07-00-07-E00062) and Yanchang Petroleum Group. J.W. acknowledges the Strategic Priority Research Program of the Chinese Academy of Sciences (XDA21000000). This work has benefited from the BL14W1 beamline at the Shanghai Synchrotron Radiation Facility and 1W1B beamline at the Beijing Synchrotron Radiation Facility. The authors thank L. Zheng for the assistance in XAS measurements.

References

- 1 F. Li, G.-F. Han, H.-J. Noh, Y. Lu, J. Xu, Y. Bu, Z. Fu and J.-B. Baek, *Angew. Chem., Int. Ed.*, 2018, **57**, 14139–14143.
- 2 J. Fester, A. Makoveev, D. Grumelli, R. Gutzler, Z. Sun, J. Rodríguez-Fernández, K. Kern and J. V. Lauritsen, *Angew. Chem., Int. Ed.*, 2018, **57**, 11893–11897.
- 3 D. Chen, M. Qiao, Y. R. Lu, L. Hao, D. Liu, C. L. Dong, Y. Li and S. Wang, *Angew. Chem., Int. Ed.*, 2018, **57**, 8691–8696.
- 4 W. Zhang, Q. Qin, L. Dai, R. Qin, X. Zhao, X. Chen, D. Ou, J. Chen, T. T. Chuong, B. Wu and N. Zheng, *Angew. Chem., Int. Ed.*, 2018, **57**, 9475–9479.
- 5 S. He, F. Ni, Y. Ji, L. Wang, Y. Wen, H. Bai, G. Liu, Y. Zhang, Y. Li, B. Zhang and H. Peng, *Angew. Chem., Int. Ed.*, 2018, **57**, 16114–16119.
- 6 C. Lv, Y. Qian, C. Yan, Y. Ding, Y. Liu, G. Chen and G. Yu, *Angew. Chem., Int. Ed.*, 2018, **57**, 10246–10250.
- 7 L. Han, S. Dong and E. Wang, *Adv. Mater.*, 2016, **28**, 9266–9291.
- 8 S. Anantharaj, S. R. Ede, K. Sakthikumar, K. Karthick, S. Mishra and S. Kundu, *ACS Catal.*, 2016, **6**, 8069–8097.
- 9 Z. Liu, Y. Wang, R. Chen, C. Chen, H. Yang, J. Ma, Y. Li and S. Wang, *J. Power Sources*, 2018, **403**, 90–96.
- 10 J. Suntivich, K. J. May, H. A. Gasteiger, J. B. Goodenough and Y. Shao-Horn, *Science*, 2011, **334**, 1383.
- 11 Y. Guo, Y. Tong, P. Chen, K. Xu, J. Zhao, Y. Lin, W. Chu, Z. Peng, C. Wu and Y. Xie, *Adv. Mater.*, 2015, **27**, 5989–5994.
- 12 Q. Shao, J. Yang and X. Huang, *Chem.–Eur. J.*, 2018, **24**, 15143–15155.
- 13 D. Yan, C.-L. Dong, Y.-C. Huang, Y. Zou, C. Xie, Y. Wang, Y. Zhang, D. Liu, S. Shen and S. Wang, *J. Mater. Chem. A*, 2018, **6**, 805–810.
- 14 P. Li, X. Duan, Y. Kuang, Y. Li, G. Zhang, W. Liu and X. Sun, *Adv. Energy Mater.*, 2018, **8**, 1703341.
- 15 X. Ou and H. Wu, *Phys. Rev. B: Condens. Matter Mater. Phys.*, 2014, **89**, 035138.
- 16 M. A. Laguna-Marco, D. Haskel, N. Souza-Neto, J. C. Lang, V. V. Krishnamurthy, S. Chikara, G. Cao and M. van Veenendaal, *Phys. Rev. Lett.*, 2010, **105**, 216407.
- 17 B. Zhang, X. Zheng, O. Voznyy, R. Comin, M. Bajdich, M. Garcia-Melchor, L. Han, J. Xu, M. Liu, L. Zheng, F. P. Garcia de Arquer, C. T. Dinh, F. Fan, M. Yuan, E. Yassitepe, N. Chen, T. Regier, P. Liu, Y. Li, P. De Luna, A. Janmohamed, H. L. Xin, H. Yang, A. Vojvodic and E. H. Sargent, *Science*, 2016, **352**, 333–337.
- 18 G. Wang, M. Zhou, J. T. Goettel, G. J. Schrobilgen, J. Su, J. Li, T. Schloder and S. Riedel, *Nature*, 2014, **514**, 475–477.
- 19 J. P. Clancy, N. Chen, C. Y. Kim, W. F. Chen, K. W. Plumb, B. C. Jeon, T. W. Noh and Y.-J. Kim, *Phys. Rev. B: Condens. Matter Mater. Phys.*, 2012, **86**, 195131.
- 20 H. Shin, H. Xiao and W. A. Goddard III, *J. Am. Chem. Soc.*, 2018, **140**, 6745–6748.
- 21 R. D. Shannon, *Acta Crystallogr., Sect. A: Cryst. Phys., Diffraction, Theor. Gen. Crystallogr.*, 1976, **32**, 751–767.
- 22 J.-H. Choy, D.-K. Kim, G. Demazeau and D.-Y. Jung, *J. Phys. Chem.*, 1994, **98**, 6258–6262.
- 23 H. N. Nong, T. Reier, H.-S. Oh, M. Gliech, P. Paciok, T. H. T. Vu, D. Teschner, M. Heggen, V. Petkov, R. Schlögl, T. Jones and P. Strasser, *Nature Catalysis*, 2018, **1**, 841–851.
- 24 X. Zheng, B. Zhang, P. De Luna, Y. Liang, R. Comin, O. Voznyy, L. Han, F. P. Garcia de Arquer, M. Liu, C. T. Dinh, T. Regier, J. J. Dynes, S. He, H. L. Xin, H. Peng, D. Prendergast, X. Du and E. H. Sargent, *Nat. Chem.*, 2018, **10**, 149–154.
- 25 M. Gorlin, P. Chernev, J. Ferreira de Araujo, T. Reier, S. Dresp, B. Paul, R. Krahnert, H. Dau and P. Strasser, *J. Am. Chem. Soc.*, 2016, **138**, 5603–5614.
- 26 N. Li, D. K. Bediako, R. G. Hadt, D. Hayes, T. J. Kempa, F. von Cube, D. C. Bell, L. X. Chen and D. G. Nocera, *Proc. Natl. Acad. Sci. U. S. A.*, 2017, **114**, 1486–1491.

- 27 D. Friebe, M. W. Louie, M. Bajdich, K. E. Sanwald, Y. Cai, A. M. Wise, M. J. Cheng, D. Sokaras, T. C. Weng, R. Alonso-Mori, R. C. Davis, J. R. Bargar, J. K. Nørskov, A. Nilsson and A. T. Bell, *J. Am. Chem. Soc.*, 2015, **137**, 1305–1313.
- 28 J. C. Conesa, *J. Phys. Chem. C*, 2016, **120**, 18999–19010.
- 29 A. J. Tkalych, K. Yu and E. A. Carter, *J. Phys. Chem. C*, 2015, **119**, 24315–24322.
- 30 M. T. Koper, *Phys. Chem. Chem. Phys.*, 2013, **15**, 1399–1407.
- 31 W. T. Hong, K. A. Stoerzinger, Y.-L. Lee, L. Giordano, A. Grimaud, A. M. Johnson, J. Hwang, E. J. Crumlin, W. Yang and Y. Shao-Horn, *Energy Environ. Sci.*, 2017, **10**, 2190–2200.
- 32 I. C. Man, H.-Y. Su, F. Calle-Vallejo, H. A. Hansen, J. I. Martínez, N. G. Inoglu, J. Kitchin, T. F. Jaramillo, J. K. Nørskov and J. Rossmeisl, *ChemCatChem*, 2011, **3**, 1159–1165.
- 33 J. Rossmeisl, Z. W. Qu, H. Zhu, G. J. Kroes and J. K. Nørskov, *J. Electroanal. Chem.*, 2007, **607**, 83–89.
- 34 A. Bergmann, E. Martinez-Moreno, D. Teschner, P. Chernev, M. Gliech, J. F. de Araujo, T. Reier, H. Dau and P. Strasser, *Nat. Commun.*, 2015, **6**, 8625.